SCIENTIFIC REPORTS

OPEN

SUBJECT AREAS:
CERAMICS
COLLOIDS

Received
3 September 2014

Accepted
2 December 2014

Published
22 January 2015

Correspondence and requests for materials should be addressed to J.C.D.D.C. (j.dacosta@eng.uq.edu.au)

Modulation of microporous/mesoporous structures in self-templated cobalt-silica

Dana L. Martens[1,2], David K. Wang[1], Julius Motuzas[1], Simon Smart[1,2] & João C. Diniz da Costa[1,2]

[1]The University of Queensland, FIMLab – Films and Inorganic Membrane Laboratory, School of Chemical Engineering, Brisbane, QLD 4072, Australia, [2]Cooperative Research Centre for Greenhouse Gas Technologies (CO2CRC).

Finite control of pore size distributions is a highly desired attribute when producing porous materials. While many methodologies strive to produce such materials through one-pot strategies, oftentimes the pore structure requires post-treatment modification. In this study, modulation of pore size in cobalt-silica systems was investigated by a novel, non-destructive, self-templated method. These systems were produced from two cobalt-containing silica starting materials which differed by extent of condensation. These starting materials, sol (SG′) and xerogel (XG′), were mixed with pure silica sol to produce materials containing 5–40 mol% Co. The resultant SG-series materials exhibited typical attributes for cobalt-silica systems: mesoporous characteristics developed at high cobalt concentrations, coinciding with Co_3O_4 formation; whereas, in the XG-series materials, these mesoporous characteristics were extensively suppressed. Based on an examination of the resultant materials a mechanism describing the pore size formation and modulation of the two systems was proposed. Pore size modulation in the XG-series was caused, in part, by the cobalt source acting as an autogenous template for the condensation of the silica network. These domains could be modified when wetted, allowing for the infiltration and subsequent condensation of silica oligomers into the pre-formed, mesoporous cages, leading to a reduction in the mesoporous content of the final product.

Designing materials with tailored pore size ranges is an integral component in the development of porous materials for various applications such as separation technologies[1–3], drug delivery[4,5] and catalysis[6–8]. For size selective separations, incorporation of multimodal[9] or hierarchical pore systems[10,11] can enhance mass transport and selectivity through the indirectly interconnected system[12,13]. Microporous materials are preferable in molecular sieving gas separations[14] and can be achieved as long as the hierarchical system contains microporous domains at the larger pore interfaces[15]. As such, a well-integrated multimodal system would provide reduced transport resistance, resulting in higher fluxes in separation processes.

Several pore size controlling systems can be employed during synthesis to tailor pore size, including chemical vapour deposition (CVD)[16], solvothermal/hydrothermal synthesis[17], and sol-gel processing[18]. Templates are often employed as structure directing agents and may be inherent[19] or used sacrificially[11,20]. However, at times these processing methods may produce pore sizes beyond the range desired. Therefore, a secondary 'healing' step may be utilised to reduce the pore size and mend defects[21]. Post-synthesis processes can also provide further functionality to the pore system[22]. Possible methods include: grafting/surface modification[23,24]; atomic layer deposition (ALD)[7,25], and embedding of organic moieties into the pores and subsequent carbonisation[26]. Previous studies in polycrystalline systems have successfully healed intercrystalline defects through the introduction of a carbon-containing entity (e.g. fluorinated organosiloxane oligomers), providing high permselectivities in ultrathin zeolite gas separation membranes[27].

Recently, there has been a burgeoning trend to incorporate transition metal ions and oxides[28–34], especially cobalt, into microporous silica systems to increase the materials' hydrothermal[34–36] or H_2S[37] stability. However, metal oxide formation can result in the formation of mesoporosity[38,39], to the detriment of the desired molecular sieving applications. While previous works have focussed more specifically on Co_3O_4 formation[40] and the hydrothermal stability of the applied materials[34–36], few have examined the mitigation of mesopore development in cobalt-silica systems.

To address the latter topic, this study departs from the conventional sol-gel method for preparing cobalt oxide silica by proposing a self-templating approach. Herein, two self-templated series were examined, the SG- and XG-series, which were prepared from mixing a pure silica sol to either an equimolar Co/Si sol (SG′) or xerogel (XG′). Further, this study investigates the impact of cobalt concentration (5–40 mol%) on the evolution of porosity of the self-templated microporous/mesoporous cobalt-silica. The physicochemical properties of these materials

were analysed by N_2 sorption, Raman spectroscopy, X-ray diffraction and transmission electron microscopy, with a mechanism proposed for the difference in textural properties obtained.

Results

The two starting material-types, sol (SG′) and xerogel (XG′), were prepared from a single-batch of equimolar Co/Si sol; where the XG′ was prepared by drying the SG′ (presented in Figure 1). The acid-catalysed SG′ consisted of partially hydrolysed oligomers up to several SiO_4^{2-} units in length (<1 nm) which were homogeneously dispersed with $[Co(H_2O)_6]^{2+}$ ions from the dissolved $Co(NO_3)_2{\cdot}6H_2O$. Upon drying to form the XG′, the silica oligomers condensed into a semi-rigid structure around the recrystallised $Co(NO_3)_2{\cdot}6H_2O$ domains. These proposed structures were corroborated by the Tyndall beam observations in Figure 1 and dynamic light scattering (not shown), where the lack of light scatter confirmed that the SG′ was oligomeric, while the condensed XG′ redispersed in a sol simulant strongly scattered light, indicative of large aggregates. Transmission electron microscopy (see Supplementary information S1a,b) confirmed that the XG′ was composed of a large, condensed structure homogeneously distributed with regions of short-range order, determined to be $Co(NO_3)_2{\cdot}6H_2O$ by X-ray diffraction (see Supplementary information S1c).

Raman spectroscopy was performed on the powders to determine the phase characteristics of the materials and is presented in Figure 2. The 0 mol% Co exhibits typical Raman features of pure silica with boson excitation ca. 120 cm^{-1}, deformation bands at 480 and 600 cm^{-1} (D1 and D2, respectively), Si–O–Si vibrational modes at ca. 430, 800, 910, 1060, 1180 cm^{-1}, and the Si–OH stretching mode at 980 cm^{-1} [41,42]. An emission centred at ca. 1200 cm^{-1} underlying all other vibrational bands was present in most spectra and was first observed at 5 mol% Co for both series. It was postulated that this emission was caused by an electronic interaction of unbound Co^{2+} ions within the matrix with the 633 nm irradiation causing the sample to fluoresce. In both series the silica D1 band, Si–OH and some

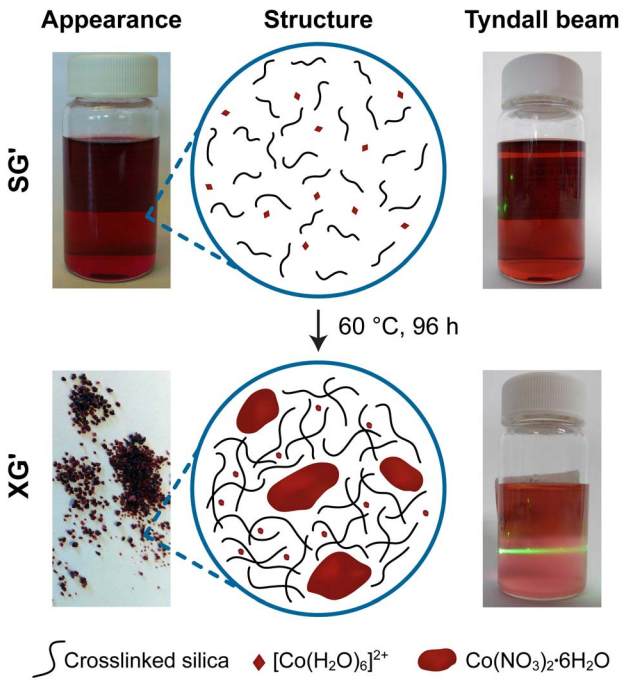

Figure 1 | Appearance, structure and Tyndall beam (L–R) of the SG′ and XG′. 20 mol% suspensions of SG′ and XG′ in a diluent of 255 EtOH : 9 HNO_3 : 40 H_2O (simulant sol solution) were used for the Tyndall beam observations. A true solution has no observable Tyndall beam (e.g. SG′).

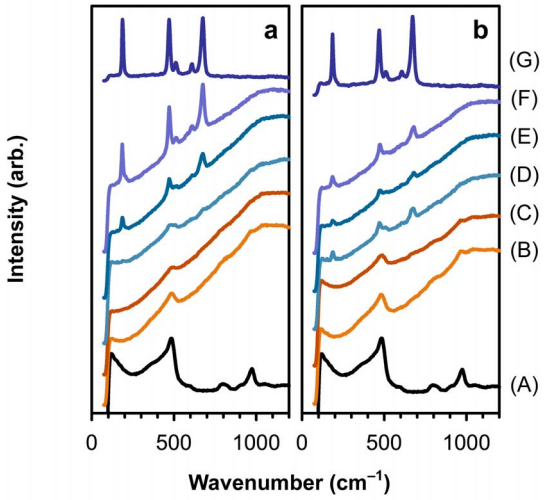

Figure 2 | Raman spectra of the (a) SG- and (b) XG-series powders, where (A) 0 mol% Co, (B) 5 mol% Co, (C) 10 mol% Co, (D) 15 mol% Co, (E) 20 mol% Co, (F) 25 mol% Co, and (G) 30 mol% Co.

Si–O–Si vibrational modes were observed to overlay the fluorescence in the 5 and 10 mol% materials. In the 15 mol% Co XG-series powder spectrum (Figure 2b, trace D), five emergent bands were at 185, 470, 510, 605 and 670 cm^{-1} were first discerned. These bands can be assigned to the five Raman-active modes, $3F_{2g}$, E_g and A_{1g}, of the normal spinel Co_3O_4 [39,43] with resonance affecting the relative intensities. In the 15 mol% SG-series spectrum (Figure 2a, trace D), these bands were also detected, albeit with only slight intensities, implying that only a small amount of Co_3O_4 had formed. From 15–25 mol% Co these characteristic Co_3O_4 bands superimposed the fluorescence suggesting that both Co^{2+} ions and Co_3O_4 were present with these samples. By 30 mol% Co, the fluorescence was quenched in both series indicating that the primary cobalt phase was Co_3O_4. No further phase changes were observed in the 35 and 40 mol% samples of either series (not shown).

The crystalline cobalt oxide phase was confirmed as Co_3O_4 (space group: Fd-3m) by X-ray diffraction, with all peaks indexed to JCPDF #76-1802, as presented in Figure 3. Crystallisation of Co_3O_4 was probed through focussed scans (34–43° 2θ) to monitor the development of the 311 reflection centred at 36.9° 2θ. As seen in Figure 3 inset (a), Co_3O_4 crystallisation was first evidenced at 20 mol% Co for the SG-series with a calculated crystallite size of 6–8 nm (15 mol% for XG-series). As the cobalt concentration was elevated to 40 mol%, the relative intensity of the 311 reflection increased and the peak sharpened, indicating an increase in Co_3O_4 crystallisation and crystallite size. Moreover, the sharp peak and broad base of the reflection at 40 mol% Co suggests a contribution from two separate crystallite distributions. The direct overlap of the peak positions made it extremely difficult to accurately determine the two distributions; however the smaller distribution was estimated to be 6–8 nm while the larger was several tens of nanometres. This dual crystallite size distribution was observed in all measured XG-series patterns as presented in Figure 3 inset (b).

Transmission electron microscopy of the 40 mol% SG- and XG-series powders confirmed the presence of multiple size distributions for the Co_3O_4 structures as detected via XRD (Figure 4). As shown in Figure 4, the SG-series material contained both large, highly-ordered structures and areas of short-range order, potentially Co_3O_4 nanocrystallites. The large six-sided polygonal-shaped Co_3O_4 particles appeared extrinsic to the amorphous silica structure and measured 40 by 60 nm (± 10 nm) on average with an aspect ratio of 0.7:1, while the regions of short-range order appeared to be contained within the amorphous network. Within these regions, lattice fringes

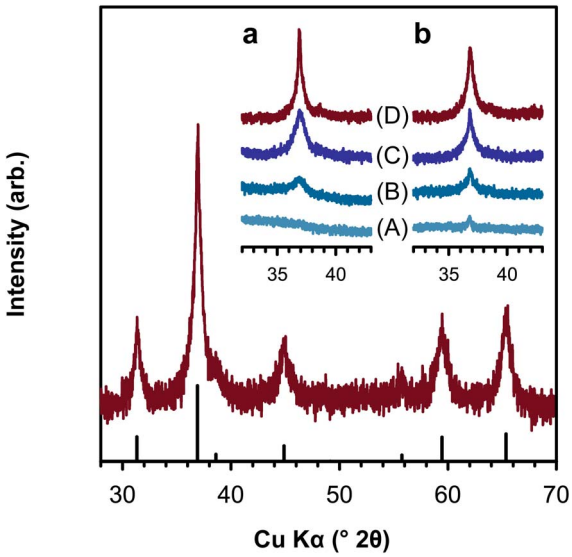

Figure 3 | XRD pattern of the 40 mol% XG-powder and JCPDF # 76-1802 stick pattern (Co_3O_4). Insets are focussed scans of the (311) reflection of the (a) SG- and (b) XG-series, where (A) 15 mol% Co, (B) 20 mol% Co, (C) 30 mol% Co, and (D) 40 mol% Co.

with interplanar distances of 0.24 nm were observed, which corresponded to the (311) d-spacings of Co_3O_4, confirming that these areas of short-range order were small Co_3O_4 nanocrystallites.

The 40 mol% XG-series powder, however, differed significantly in structure as shown in Figure 4. Namely, the large particles contained features measuring upwards of 10 × 12 nm, which were aligned to the Co_3O_4 crystal planes (Figure 4d,e). It was postulated that these features were topographic depressions as the lighter shading of these regions suggests the electron beam was transmitted through a thinner cross-section of material. There was also limited evidence to indicate that the features were within the crystal (e.g. voids) as there was no corresponding mesoporosity observed in the nitrogen sorption (discussed later). Furthermore, the orientation and geometry of these defects suggests a stacking fault may have occurred during crystallisation resulting in the formation of a hexagonal valley in-plane with the crystal face. Compared to their SG-series counterparts, these large particles varied greater in size distribution, although they maintained an aspect ratio of ca. 0.7:1. The small Co_3O_4 nanocrystallites in the XG-series powder (Figure 4f) were more distinct than those observed for the SG-series powder (Figure 4c) and also appeared to be embedded within the silica matrix.

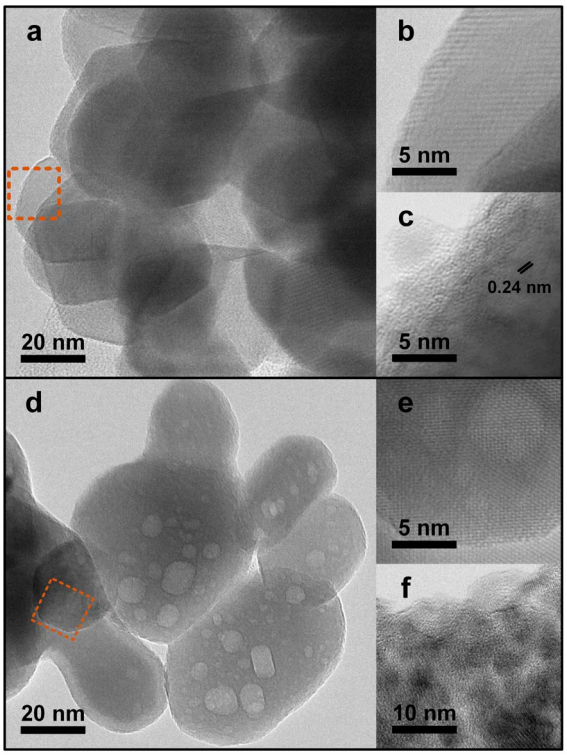

Figure 4 | Transmission electron micrographs of the 40 mol% SG-powder, (a) large particles, (b) high-resolution of large particle, and (c) small particles; and 40 mol% XG-powder, (d) large particles, (e) high-resolution of large particle, and (f) small particles.

After confirming that the Co_3O_4 crystallisation was essentially equivalent in both the SG- and XG-systems, nitrogen sorption was employed to determine the influence of the preparation method on the formation of the porous silica matrix. Figure 5 shows the nitrogen isotherms for the calcined powders. The SG-series powders, presented in Figure 5a exhibited typical Type I isotherms (microporous materials) at low cobalt concentrations, developing Type IV characteristics (mesoporous materials) at high cobalt concentrations (>35 mol%). More specifically, the powders containing 5–15 mol% Co presented Type I isotherms with decreasing quantities of nitrogen adsorbed, substantially less than pure silica (0 mol% Co), and no hysteresis. From 20 mol% Co upwards, there was an escalation in multilayer adsorption coinciding with increasing cobalt concentration. H2 hysteresis was first observed at 25 mol% Co, a characteristic of mesoporous materials, developing substantially from 30–40 mol% Co. These observations are typically observed in cobalt-silica materials[38,44], especially at high cobalt concentrations, and suggest that the mixing of pre-hydrolysed sols employed in this study had no influence on the final materials. The sorption isotherms of the XG-series powders differed significantly with Type I characteristics retained over the full concentration range, as shown in Figure 5b. Likewise to the SG-series, the quantity adsorbed decreased with increasing cobalt content from 5–25 mol%, with slight multilayer adsorption occurring from 30–40 mol% Co. Narrow H2 hysteresis was observed in most samples.

As observed in Figure 6a, the specific surface areas of the materials decreased from the pure silica (540 m^2/g), upon addition of cobalt for both series. For the SG-series, the surface area reduced considerably (ca. 130 m^2/g) for the 5 mol% Co sample before further decreasing and then stabilising at 370 ± 20 m^2/g from 10–40 mol% Co. In comparison, the surface areas of the XG-series continued to decrease across the entire concentration range, correlating closely to the reduced quantities adsorbed in the respective isotherms. The pore volumes in Figure 6b trended similarly to the respective surface areas for both series, albeit with variance in the high cobalt concentrations. In the SG-series, an initial pore volume decrease was observed at low concentrations (markedly between 0 and 5 mol%), followed by a steady rise in pore volume before stabilising at 35–40 mol%. The XG-series, however, consistently decreased in pore volume from 0–20 mol% before stabilising over 25–40 mol% Co. The increasing pore volume at high cobalt concentrations in the SG-series coincides with the large hysteresis observed in the isotherms, suggesting that larger pores attributed to the increase in pore volume. These results indicate that there was a strong correlation between the surface areas and pore volumes of these materials, though this relationship was not directly proportional (especially in the SG-series).

The pore size distributions (PSD) based on density functional theory (DFT) for all samples are displayed in Figure 7 with the relative pore volume contributions presented in Figure 8. The PSD traces contained up to seven distinct pore size contributions, depending on the cobalt concentration. These contributions were centred at 15, 20, 24, 33, 48 and 57 Å, with the seventh unresolved contribution

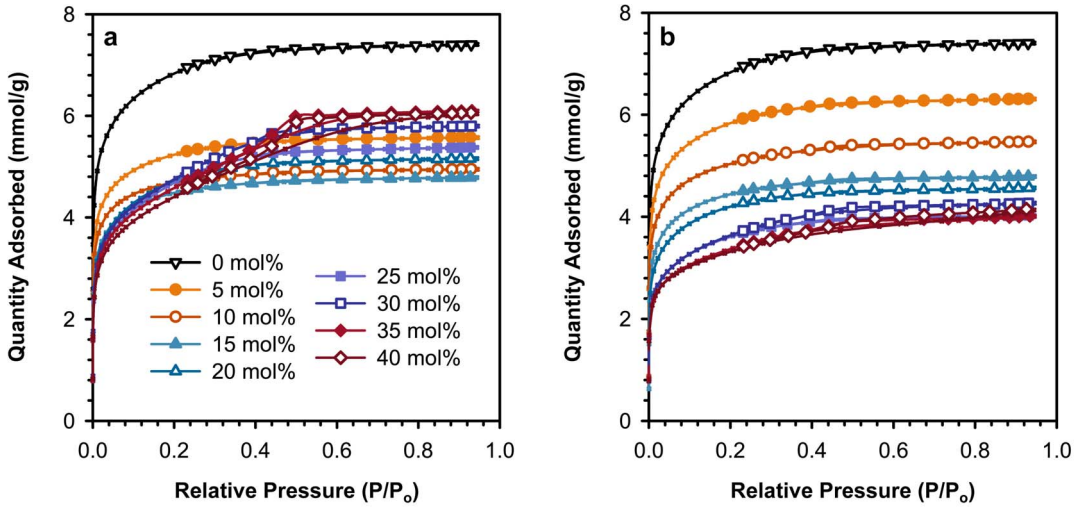

Figure 5 | Nitrogen sorption isotherms of (a) SG- and (b) XG-series powders. Symbols: small symbols on adsorption branch; large, identifier symbols on desorption branch.

centred below 14 Å. In these materials, the 20 Å pore size was the primary contributor towards the measured pore volume for most samples. Pure amorphous silica systems are known to have a trimodal pore size distribution[45], hence the addition of cobalt oxide through the SG′ and XG′ to silica matrices have created interfaces with varying pore sizes otherwise not found in pure silica samples. As seen for the pure silica powder (trace A, Figures 7a,b), five modelled pore sizes contributed to the measured pore volume. The predominance of measured volume was attributed to the 20 Å and shouldering 24 Å pore size (ca. 57%), with small contributions from the 15, 33 and >387 Å pores (ca. 5–8% each), and a significant proportion from pores ≤14 Å (ca. 25%). As cobalt was added to the silica system in the SG-series, the 33 Å pore size diminished from 5 mol% Co until the cobalt concentration reached 20 mol% (traces B–E, Figure 7a). As the concentration was raised beyond 20 mol%, both the breadth of distribution and corresponding volume adsorbed by the 33 Å pore size increased considerably, as observed Figure 7a, traces E–I. The re-emergence of these pore sizes and associated pore volumes can be attributed to the enhanced multilayer adsorption observed in the adsorption isotherms and accompanying increase in pore volumes between 20–40 mol% Co (Figures 5a and 6b, respectively). In the materials containing 35 and 40 mol% Co, the emergent, sharp 48 Å pore and broad distribution centred at 57 Å were consistent with the development of Type IV characteristics in the corresponding isotherms (Figure 5a).

Conversely, the development of large pores was reduced in the XG-series. While 33 Å pores were noted for the 5–20 mol% materials (traces B–E, Figure 7b), the relative pore volume contributions remained ca. 5% or less. As the cobalt concentration was increased from 25–40 mol% this pore size contribution broadened, with small contributions centred at 48 and 57 Å present from 30 mol% onwards. Over the 20–40 mol% range, the relative pore volume of these larger pores increased from 5–20% for the XG-series compared with ca. 8–40% for the SG-series over the same range. The smaller contribution of large pores is represented in the respective isotherms in Figure 7b, with diminishing quantities adsorbed and reduced Type IV characteristics compared to the SG-series.

Discussion

Starting material-type, as well as cobalt concentration had a strong effect on the physiochemical properties of the materials investigated in this study. While producing materials with consistent specific

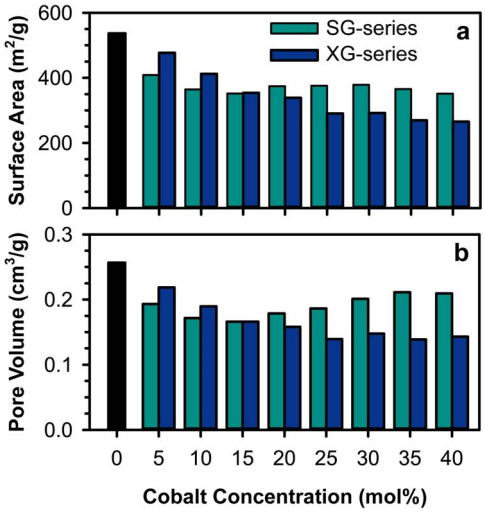

Figure 6 | (a) Specific surface areas and (b) total pore volumes of the SG- and XG-series powders.

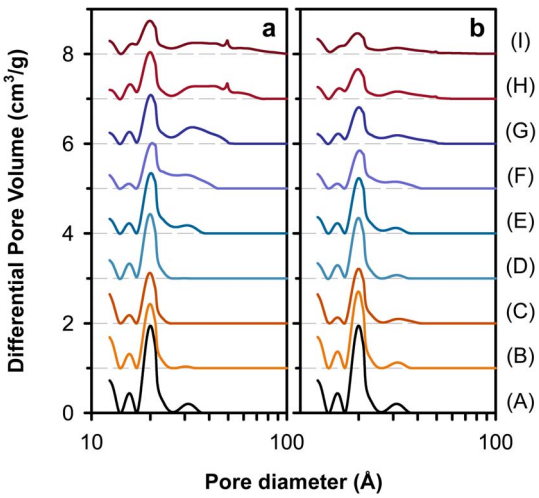

Figure 7 | DFT pore size distributions of the (a) SG- and (b) XG-series powders, where (A) 0 mol% Co, (B) 5 mol% Co, (C) 10 mol% Co, (D) 15 mol% Co, (E) 20 mol% Co, (F) 25 mol% Co, (G) 30 mol% Co, (H) 35 mol% Co and (I) 40 mol% Co. Each trace is offset by 1 cm^3/g.

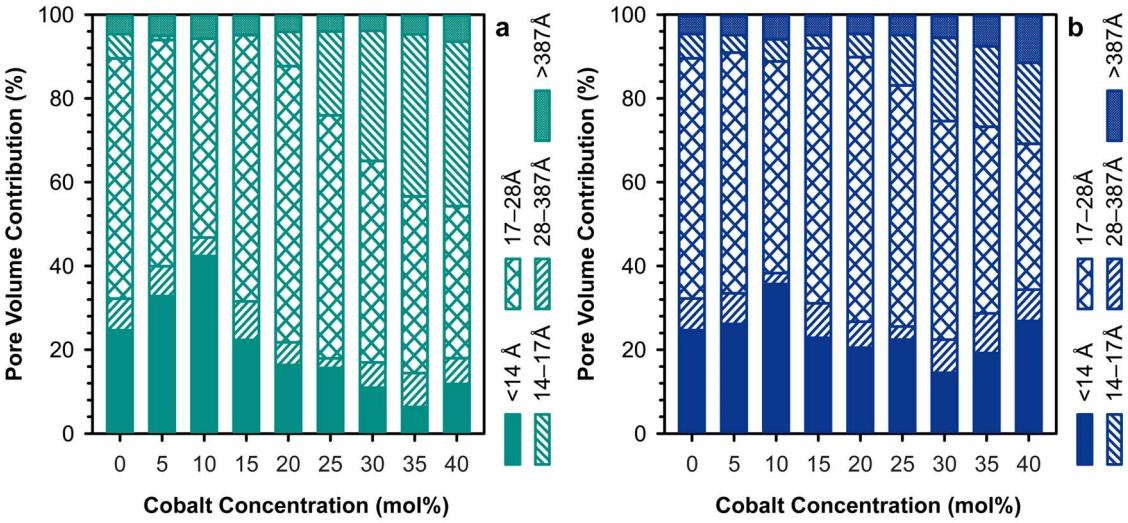

Figure 8 | Relative pore volume contributions for the (a) SG-and (b) XG-series. Pore size ranges: <14 Å, 14–17 Å, 17–28 Å, 28–387 Å, >387 Å. The 28–387 Å range contains the 33, 48, 57 Å pore size contributions.

surface areas across a broad range of concentrations (10–40 mol% Co, Figure 6a), the textural properties of the SG-series powders evolved as the cobalt concentration was increased. Initially forming microporous materials with strong Type I characteristics at low concentrations, the SG-series powders developed Type IV mesoporous attributes at high concentrations (Figure 5a). These materials retained a considerable microporous component with the additional formation of a mesoporous distribution (upwards of 100 Å), effectively increasing the pore volume (Figure 7a). Comparatively, the pre-condensed structure employed in the XG-series exerted a modulating effect on the development of mesopores, with Type I characteristics maintained across the whole concentration range (Figure 5b). This was most evident in materials containing 25–40 mol% Co, where the formation of mesopores > 24 Å was suppressed; coincidently with a concurrent reduction in 20–24 Å pores (Figure 7b). This reduced development of pores affected both the specific surface areas and pore volumes for these XG-series materials.

Crystallisation of Co_3O_4 was evidenced in both series when moderate cobalt concentrations were employed (15–20 mol%), with Co_3O_4 crystallising at lower cobalt concentrations in the XG-series (Figure 3). The crystallisation of Co_3O_4 coincided with the escalation of multilayer adsorption[44] in the SG-series at 20 mol%, but not in the XG-series (Figure 5). Rather, the influence of Co_3O_4 on the XG-series' isotherms was not observed until 30 mol% Co where multilayer adsorption and enhanced hysteresis occurred. The starting material-type also influenced the crystallite distributions produced, with a single distribution of small crystallites observed for most SG-series materials (exception: 40 mol%), and a binary system containing small and large crystallites detected in the XG-series. This binary distribution of particle sizes was also observed in the TEM for the 40 mol% samples in both series (Figure 4). These large, highly crystalline Co_3O_4 were observed towards the extremities of the silica agglomerates implicating formation through Ostwald ripening.

To elucidate the difference in final structure, the characteristics of the pre-condensed xerogel structure employed in the XG-series should be considered and are schematically represented in Figure 9. As previously observed by TEM and XRD (Supplementary information Figure S1), the dried XG′ contained $Co(NO_3)_2{\cdot}6H_2O$ crystals homogenously distributed through the condensed silica network (Figure 9 (A)). The integrity of the silica network in the uncalcined XG′ was inspected by filtering the 20 mol% XG′ suspension employed for the Tyndall beam observation (Figure 1). The resultant powder (washed-XG′, Figure 9 (C)) was white with a very faint pink tint, while the filtrate was richly hued indicating that the $Co(NO_3)_2{\cdot}6H_2O$ crystals were readily solubilised in the simulant sol solution. The yield of washed-XG′ reclaimed equated to the stoichiometric quantity of SiO_2 contained within the XG′; indicating that only $Co(NO_3)_2{\cdot}6H_2O$ was solubilised. The morphology of the washed-XG′ presented an intricate, convoluted structure that was devoid of the short-range order observed prior to washing where cavities remained in lieu of the crystalline component (Figure 9 (C) and (D), for TEM see Supplementary information S2). Negligible cobalt was detected by energy-dispersive X-ray analysis (not shown) indicating that the majority of cobalt had been removed. The textural properties of the calcined, washed-XG′ were examined by nitrogen sorption, whereby a Type IV isotherm (mainly mesoporous) with a considerable surface area of ca. 700 m^2/g were observed (see Supplementary information S3, trace D). This isotherm exhibited strong multilayer adsorption and H2 hysteresis, with an adsorption profile similar to the calcined XG′, though with a greater quantity adsorbed. The PSD of the washed-XG′ also showed an appreciable increase in breadth and contribution of pores > 20 Å, especially pores > 50 Å. These results strongly implicate that the $Co(NO_3)_2{\cdot}6H_2O$ crystals act as self-templating agents for the silica matrix, which condenses around the crystal domains. During calcination, further condensation of the silica matrix would be promoted, stabilising these mesostructured cages. Furthermore, shrinkage of the unit cell volume of $Co(NO_3)_2{\cdot}6H_2O$ crystal (JCPDF #25-1219) as it oxidises to cubic Co_3O_4 (JCPDF #76-1802) during calcination from 1024 to 526 $Å^3$ and would create a cavity in this mesostructured cage, providing the calcined XG′ with its Type IV characteristics. This in turn would reduce the apparent pore size of the mesostructured cage when compared to the washed-XG′ (Figure 9 (B) vs. (D)).

Thus, the difference in textural properties in the two series can be explained by the structure-directing properties imparted by $Co(NO_3)_2{\cdot}6H_2O$ recrystallisation during the drying process; supporting the case for the proposed self-templated approach in this work. As presented in the Figure 10 schematic, mixing the pure silica sol with the SG′ produces a homogeneous solution with greater silica content. Upon drying, the silica network would condense around the recrystallised $Co(NO_3)_2{\cdot}6H_2O$, likewise to the XG′, forming a similar mesoporous structure after calcination. This similarity is corroborated by the analogous isotherms of the 40 mol% SG-powder and the calcined XG′, where the former exhibited a greater quantity adsorbed (see Supplementary information S3, traces A and B).

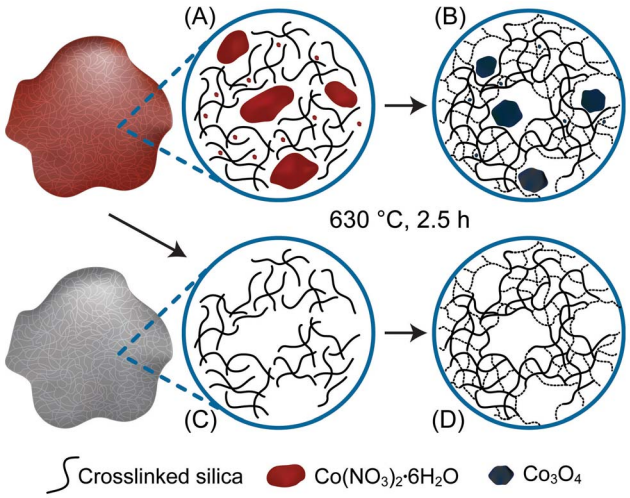

Figure 9 | Structural non-idealised schematic of the XG′ (A) dried [as-prepared], (B) calcined, (C) washed, (D) washed and calcined. The $Co(NO_3)_2 \cdot 6H_2O$ crystals in the XG′ act as structure-directing agents for the silica network. The extended condensed silica network is represented by dashed lines.

Comparing this to the 40 mol% XG-powder (trace C), produced from the dried XG′, the mesoporous characteristic had been dramatically subdued. As previously demonstrated, the $Co(NO_3)_2 \cdot 6H_2O$ contained within the XG′ dissolves when the XG′ is wetted. Therefore, addition of pure silica sol to the XG′ would dissolve the $Co(NO_3)_2 \cdot 6H_2O$ crystals allowing the infiltration of silica oligomers into the mesostructured cages whilst allowing for a homogeneous redispersion of the $[Co(H_2O)_6]^{2+}$ throughout the silica network. When the material was then dried, the extra silica oligomers present in the mesostructured cages would condense, confining the recrystallisation of $Co(NO_3)_2 \cdot 6H_2O$, leading to the formation of smaller crystalline domains and narrower pore size distributions. Smaller localised domains of cobalt would thus lead to smaller Co_3O_4 crystallites. These smaller crystallites would be more susceptible to Ostwald ripening, providing greater potential of forming a binary crystallite distribution; as observed for the XG-series. In essence, the $Co(NO_3)_2 \cdot 6H_2O$ acts as a self-template for the condensation of the silica matrix. The $Co(NO_3)_2 \cdot 6H_2O$ can either be removed or redistributed throughout the system through post-treatments, allowing for the formed, mesostructured cage to be modified, thus providing a mechanism for pore size modulation and mesopore mitigation.

The crystalline domain size of the $Co(NO_3)_2 \cdot 6H_2O$ could potentially influence the crystallisation and conversion of the Co specie to Co_3O_4. In both series, Co_3O_4 was initially detected by XRD between 15 and 20 mol% Co (Figure 3) which implies that the $Co(NO_3)_2 \cdot 6H_2O$ crystalline domain size below these cobalt concentrations was insufficient to yield Co_3O_4 crystallites of detectable size. Moreover, the fluorescence observed in the Raman spectroscopy (Figure 4) for materials containing 5–25 mol% Co indicates an electronic interaction occurred with the cobalt, which possibly remained in the ionic state. This suggests that these cobalt atoms may have been confined within the silica matrix inhibiting them from diffusing to the cobalt rich $Co(NO_3)_2 \cdot 6H_2O$ domains. Such atoms may have been responsible for the pale pink hue in the washed-XG′. The cobalt speciation in these materials was not further investigated in this study.

In summary, infiltration of a hydrolysed silica sol into a pre-condensed, self-templated silica structure such as the XG′ allows for modulation of previously generated porosities; effectively suppressing the mesoporous character in high cobalt-containing cobalt-silica systems. This provides a potential 'healing' mechanism for the pore system and could increase the likelihood of a continuous microporous domain at the larger pore interfaces; a key criteria for multimodal and hierarchical systems for use in size selective applications. However, this moderation of pore size comes at the expense of the pore volume which could affect the mass transport through the system, though to a much lesser extent than a continuous microporous system.

Methods

Pure silica and a cobalt-silica sols (Co/Si 1 : 1) were prepared by the following molar ratio regimen : 255 EtOH : 4 TEOS : 0 or 4 $Co(NO_3)_2 \cdot 6H_2O$: 9 HNO_3 : 40 H_2O. Briefly, cobalt nitrate hexahydrate (Alfa Aesar, ACS, 98–102%) was dissolved in absolute ethanol under stirring, followed by addition of water and nitric acid (ACI Scan, 70%). The reaction mixture was equilibrated in an ice-bath prior to the dropwise addition of tetraethyl orthosilicate TEOS (Aldrich, 98%), and maintained under stirring for 3 h at 0°C. The single-batch, equimolar Co/Si sol was subsampled to produce the two starting materials, herein referred to as SG′ and XG′, which differed by extent of condensation. The SG′ comprised of the as-synthesised sol and was refrigerated to minimise further polymerisation, while the XG′ was oven-dried at 60°C for 96 h to form a xerogel. The XG′ was then finely ground and stored in a vacuum desiccator until use.

To minimise experimental variation, solutions containing 5–40 mol% Co in SiO_2 were prepared by mixing the SG′ and XG′ with aliquots of a large-scale batch of pure silica sol. The required quantities of SG′- or XG′-to-pure silica sol were determined through balancing the mole/total mass ratios of the Co and Si contained in the SG′,

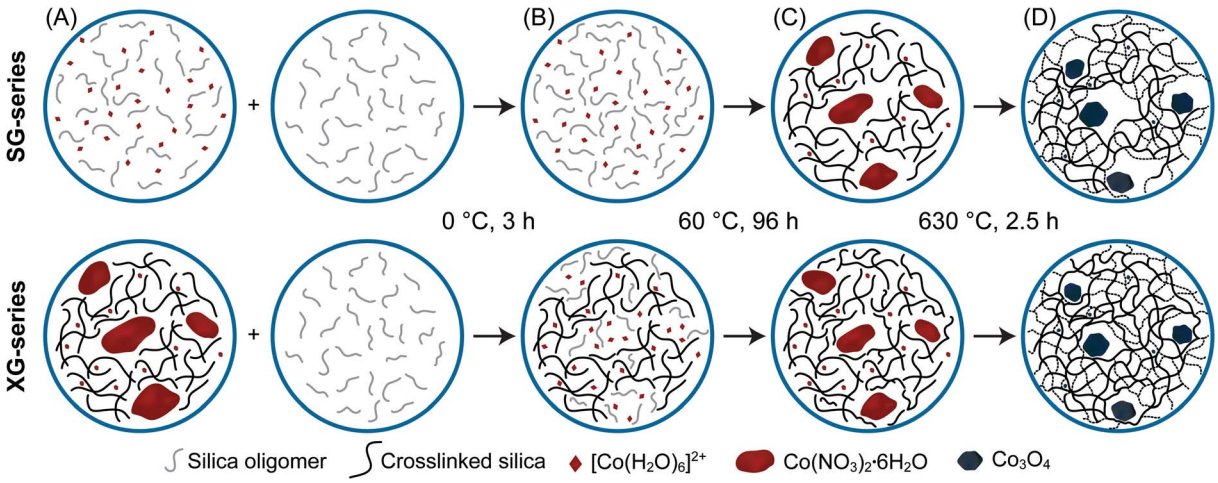

Figure 10 | Non-idealised schematic of material formation for the SG- and XG-series through the stages of (A) starting materials, (B) mixing, (C) drying, and (D) calcination. The extended condensed silica network is represented by dashed lines.

XG′ and pure silica sol. Upon addition of the silica sol to the SG′ or XG′, the sol was stirred for 3 h at 0°C in an ice bath. Afterwards, the sols were oven-dried at 60°C for 96 h prior to calcination at 630°C for 2.5 h employing heating and cooling rates of 1 and 2°C min^{-1}, respectively. All powders were produced within 0.02% of the desired mol% Co concentration. After drying and calcination, the remaining pure silica sol was investigated as the 0 mol% Co sample. The materials are referred in the text as per their starting material-type, SG or XG, and their cobalt concentrations in mol%. The SG-series represents materials produced through the standard hydrolysis of TEOS in the presence of $Co(NO_3)_2 \cdot 6H_2O$.

Nitrogen sorption measurements over a relative pressure range of 0.0005–0.95 P/P_o were performed on a Micromeritics TriStar 3000 analyser after degassing at 200°C overnight under vacuum on a VacPrep061. Specific surface area measurements were calculated by Brunner-Emmett-Teller (BET) model from adsorption data in the 0.05–0.20 relative pressure range. Single point pore volume measurements (ca. 0.94 P/P_o) were confirmed with the limiting micropore volume determined through the Dubunin-Astakov (DA) model (correlation within 1% of the reported single point value). Pore diameters were determined via density functional theory (DFT) modelling of the entire adsorption branch (0.0005–0.95 P/P_o), employing a model based on N_2 sorption on a metal oxide with cylindrical pores, utilising a regularisation factor of 0.40. The minimum size modelled by DFT (12 Å) was limited by the initial relative pressures measured (ca. 5×10^{-4} P/P_o). The relative pore size contributions (%) were estimated for the following ranges ≤14 Å, 14–17 Å, 17–28 Å, and 28–387 Å. The relative contributions were calculated from the DFT-modelled, cumulative volumes adsorbed at the range's upper limit (e.g. 14 Å) as a fraction of the total pore volume measured (single point measurement).

X-ray diffraction (XRD) was conducted on a Bruker D8 Advance with a graphite monochromator using Cu Kα radiation operating at 40 mA and 40 kV over 20–70° 2θ at a step size of 0.02° 2θ. High-resolution (narrow) scans were collected between 32 to 43° 2θ at a step size of 0.01° 2θ and a scanning rate of 1.9 s/step. Crystallite sizes were estimated using the Scherrer equation on the $K\alpha_2$-stripped narrow scans, employing a Pearson VII peak-shape to fit the Co_3O_4 (311) reflection centred at 36.9° 2θ. Transmission electron microscopy (TEM) images were obtained on a JEOL 2010 electron microscope with an acceleration voltage of 200 kV. TEM grids were prepared by drop-casting an aliquot of xerogel suspension onto a lacey carbon film (Beijing XXBR Technology Co., Ltd, China) and air-dried. Raman spectra were acquired with a Nicolet Almega XR dispersive Raman spectrometer coupled to an Olympus microscope using a He:Ne laser (633 nm) over 3900–70 cm^{-1}.

1. Pendergast, M. M. & Hoek, E. M. V. A review of water treatment membrane nanotechnologies. *Energy Environ. Sci.* **4**, 1946–1971 (2011).
2. Nawrocki, J., Dunlap, C., McCormick, A. & Carr, P. W. Part I. Chromatography using ultra-stable metal oxide-based stationary phases for HPLC. *J. Chromatogr., A* **1028**, 1–30 (2004).
3. Miller, C. R., Wang, D. K., Smart, S. & Diniz da Costa, J. C. Reversible redox effect on gas permeation of cobalt doped ethoxy polysiloxane (ES40) membranes. *Sci. Rep.* **3**, 1648, doi:10.1038/srep01648 (2013).
4. Arruebo, M. Drug delivery from structured porous inorganic materials. *Wiley Interdiscip. Rev. Nanomed. Nanobiotechnol.* **4**, 16–30 (2012).
5. Qu, F. *et al.* Controlled release of Captopril by regulating the pore size and morphology of ordered mesoporous silica. *Microporous Mesoporous Mater.* **92**, 1–9 (2006).
6. Frenzer, G. & Maier, W. F. Amorphous porous mixed oxides: Sol-gel ways to a highly versatile class of materials and catalysts. *Annu. Rev. Mater. Res.* **36**, 281–331 (2006).
7. Detavernier, C., Dendooven, J., Pulinthanathu Sree, S., Ludwig, K. F. & Martens, J. A. Tailoring nanoporous materials by atomic layer deposition. *Chem. Soc. Rev.* **40**, 5242–5253 (2011).
8. Zubir, N. A., Yacou, C., Motuzas, J., Zhang, X. & Diniz da Costa, J. C. Structural and functional investigation of graphene oxide–Fe_3O_4 nanocomposites for the heterogeneous Fenton-like reaction. *Sci. Rep.* **4**, 4594, doi: 10.1038/srep04594 (2014).
9. Ahmad, A. L., Leo, C. P. & Abd. Shukor, S. R. Tailoring of a γ-Alumina Membrane with a Bimodal Pore Size Distribution for Improved Permeability. *J. Am. Ceram. Soc.* **91**, 246–251 (2008).
10. Backov, R. Combining soft matter and soft chemistry: integrative chemistry towards designing novel and complex multiscale architectures. *Soft Matter* **2**, 452–464 (2006).
11. Innocenzi, P., Malfatti, L. & Soler-Illia, G. J. A. A. Hierarchical mesoporous films: From self-assembly to porosity with different length scales. *Chem. Mater.* **23**, 2501–2509 (2011).
12. Yuan, Z.-Y. & Su, B.-L. Insights into hierarchically meso-macroporous structured materials. *J. Mater. Chem.* **16**, 663–677 (2006).
13. Ayral, A. Colloids for Nano- and Biotechnology in *Progress in Colloid and Polymer Science*. (eds Hórvölgyi, Z. D. & Kiss, É) 1–90 (Springer Berlin - Heidelberg, 2008).
14. Lu, G. Q. *et al.* Inorganic membranes for hydrogen production and purification: A critical review and perspective. *J. Colloid Interface Sci.* **314**, 589–603 (2007).
15. Yacou, C., Ayral, A., Giroir-Fendler, A., Fontaine, M.-L. & Julbe, A. Hierarchical porous silica membranes with dispersed Pt nanoparticles. *Microporous Mesoporous Mater.* **126**, 222–227 (2009).
16. Lin, Y. S. & Burggraaf, A. J. CVD of solid oxides in porous substrates for ceramic membrane modification. *AIChE J.* **38**, 445–454 (1992).
17. Fulvio, P. F., Pikus, S. & Jaroniec, M. Tailoring properties of SBA-15 materials by controlling conditions of hydrothermal synthesis. *J. Mater. Chem.* **15**, 5049–5053 (2005).
18. Brinker, C. J. *et al.* Sol-gel strategies for controlled porosity inorganic materials. *J. Membr. Sci.* **94**, 85–102 (1994).
19. Guo, Z., Du, F., Li, G. & Cui, Z. Controlled synthesis of mesoporous SiO_2/$Ni_3Si_2O_5(OH)_4$ core-shell microspheres with tunable chamber structures via a self-template method. *Chem. Commun.* **25**, 2911–2913 (2008).
20. Wang, D., Caruso, R. A. & Caruso, F. Synthesis of macroporous titania and inorganic composite materials from coated colloidal spheres: A novel route to tune pore morphology. *Chem. Mater.* **13**, 364–371 (2001).
21. Koutsonikolas, D. *et al.* Defects in microporous silica membranes: Analysis and repair. *Sep. Purif. Technol.* **73**, 20–24 (2010).
22. Angelomé, P. C. & Soler-Illia, G. J. d. A. A. Organically modified transition-metal oxide mesoporous thin films and xerogels. *Chem. Mater.* **17**, 322–331 (2005).
23. Kruk, M., Antochshuk, V., Matos, J. R., Mercuri, L. P. & Jaroniec, M. Determination and tailoring the pore entrance size in ordered silicas with cage-like mesoporous structures. *J. Am. Chem. Soc.* **124**, 768–769 (2002).
24. Choi, M. *et al.* Controlled polymerization in mesoporous silica toward the design of organic−inorganic composite nanoporous materials. *J. Am. Chem. Soc.* **127**, 1924–1932 (2005).
25. Li, F., Yang, Y., Fan, Y., Xing, W. & Wang, Y. Modification of ceramic membranes for pore structure tailoring: The atomic layer deposition route. *J. Membr. Sci.* **397–398**, 17–23 (2012).
26. Duke, M. C., Diniz da Costa, J. C., Do, D. D., Gray, P. G. & Lu, G. Q. Hydrothermally robust molecular sieve silica for wet gas separation. *Adv. Funct. Mater.* **16**, 1215–1220 (2006).
27. Drobek, M. *et al.* Evaluation of a new supercritical CO_2-assisted deposition method for preparing gas selective polymer/zeolite composite membranes. *J. Membr. Sci.* **429**, 428–435 (2013).
28. Boffa, V. *et al.* Toward the effective design of steam-stable silica-based membranes. *Microporous Mesoporous Mater.* **179**, 242–249 (2013).
29. Gu, Y. & Oyama, S. T. Permeation properties and hydrothermal stability of silica–titania membranes supported on porous alumina substrates. *J. Membr. Sci.* **345**, 267–275 (2009).
30. Yoshida, K., Hirano, Y., Fujii, H., Tsuru, T. & Asaeda, M. Hydrothermal stability and performance of silica-zirconia membranes for hydrogen separation in hydrothermal conditions. *J. Chem. Eng. Jpn.* **34**, 523–530 (2001).
31. Kanezashi, M. & Asaeda, M. Hydrogen permeation characteristics and stability of Ni-doped silica membranes in steam at high temperature. *J. Membr. Sci.* **271**, 86–93 (2006).
32. Ballinger, B., Motuzas, J., Smart, S. & Diniz da Costa, J. C. Palladium cobalt binary doping of molecular sieving silica membranes. *J. Membr. Sci.* **451**, 185–191 (2014).
33. Wang, D. K., Diniz da Costa, J. C. & Smart, S. Development of rapid thermal processing of tubular cobalt oxide silica membranes for gas separations. *J. Membr. Sci.* **456**, 192–201 (2014).
34. Liu, L. *et al.* Physicochemical characterisation and hydrothermal stability investigation of cobalt-incorporated silica xerogels. *RSC Adv.* **4**, 18862–18870 (2014).
35. Igi, R., Yoshioka, T., Ikuhara, Y. H., Iwamoto, Y. & Tsuru, T. Characterization of Co-doped silica for improved hydrothermal stability and application to hydrogen separation membranes at high temperatures. *J. Am. Ceram. Soc.* **91**, 2975–2981 (2008).
36. Uhlmann, D., Liu, S., Ladewig, B. P. & Diniz da Costa, J. C. Cobalt-doped silica membranes for gas separation. *J. Membr. Sci.* **326**, 316–321 (2009).
37. Uhlmann, D., Smart, S. & Diniz da Costa, J. C. H_2S stability and separation performance of cobalt oxide silica membranes. *J. Membr. Sci.* **380**, 48–54 (2011).
38. Esposito, S. *et al.* Cobalt–silicon mixed oxide nanocomposites by modified sol–gel method. *J. Solid State Chem.* **180**, 3341–3350 (2007).
39. Santos, G. A., Santos, C. M. B., da Silva, S. W., Urquieta-González, E. A. & Sartoratto, P. P. C. Sol–gel synthesis of silica–cobalt composites by employing Co_3O_4 colloidal dispersions. *Colloids Surf., A* **395**, 217–224 (2012).
40. Olguin, G., Yacou, C., Smart, S. & Diniz da Costa, J. C. Tailoring the oxidation state of cobalt through halide functionality in sol-gel silica. *Sci. Rep.* **3**, 2449, doi:10.1038/srep02449 (2013).
41. Bertoluzza, A., Fagnano, C., Antonietta Morelli, M., Gottardi, V. & Guglielmi, M. Raman and infrared spectra on silica gel evolving toward glass. *J. Non-Cryst. Solids* **48**, 117–128 (1982).
42. Duverger, C. *et al.* Waveguide Raman spectroscopy: a non-destructive tool for the characterization of amorphous thin films. *J. Mol. Struct.* **480–481**, 169–178 (1999).
43. Hadjiev, V. G., Iliev, M. N. & Vergilov, I. V. The Raman spectra of Co_3O_4. *J. Phys. C: Solid State Phys.* **21**, L199–L201 (1988).
44. Esposito, S. *et al.* Sol-gel synthesis of silicon cobalt mixed oxide nanocomposites. *Chem. Eng. Trans.* **11**, 83–88 (2007).
45. Duke, M. C., Pas, S. J., Hill, A. J., Lin, Y. S. & Diniz da Costa, J. C. Exposing the molecular sieving architecture of amorphous silica using positron annihilation spectroscopy. *Adv. Funct. Mater.* **18**, 3818–3826 (2008).

Acknowledgments

The authors would like to acknowledge financial support provided by the Australian Government through its CRC program to support this CO2CRC research project. The authors acknowledge the facilities, and the scientific and technical assistance, of the Australian Microscopy & Microanalysis Research Facility at the Centre for Microscopy and

Microanalysis, The University of Queensland. Raman spectroscopy was performed at the Bio-Nano Development Facility in the Australian Institute for Bioengineering and Nanotechnology, which was funded by the Queensland State Government Smart State Innovation Building Fund. JCDdC acknowledges support from the Australian Research Council Future Fellowship program (FT130100405).

Author contributions

D.L.M. performed all experiments and prepared the manuscript including figures and supplementary analysis. J.M. performed T.E.M. measurements. D.K.W., J.M., S.S. and J.C.d.C. helped develop the experimental design and contributed to the analysis and discussion of the results. All authors reviewed the final manuscript before submission.

Additional information

Supplementary information accompanies this paper at http://www.nature.com/scientificreports

Competing financial interests: The authors declare no competing financial interests.

How to cite this article: Martens, D.L., Wang, D.K., Motuzas, J., Smart, S. & Diniz da Costa, J.C. Modulation of microporous/mesoporous structures in self-templated cobalt-silica. *Sci. Rep.* **5**, 7970; DOI:10.1038/srep07970 (2015).

This work is licensed under a Creative Commons Attribution-NonCommercial-NoDerivs 4.0 International License. The images or other third party material in this article are included in the article's Creative Commons license, unless indicated otherwise in the credit line; if the material is not included under the Creative Commons license, users will need to obtain permission from the license holder in order to reproduce the material. To view a copy of this license, visit http://creativecommons.org/licenses/by-nc-nd/4.0/